ADVANCED OPTICAL MATERIALS
www.advopticalmat.de

Efficient Er/O-Doped Silicon Light-Emitting Diodes at Communication Wavelength by Deep Cooling

Huimin Wen, Jiajing He, Jin Hong, Shenbao Jin, Zhenming Xu, Hong Zhu, Jingquan Liu, Gang Sha, Fangyu Yue, and Yaping Dan**

A silicon light source at the communication wavelength is the bottleneck for developing monolithically integrated silicon photonics. Doping silicon with erbium and oxygen ions is considered one of the most promising approaches to produce silicon light sources. However, this method suffers from a high concentration of defects in the form of nonradiative recombination centers at the interface between the crystalline silicon and large $Er_2O_3/ErSi_{1.7}$ precipitates during the standard rapid thermal treatment. Here, a deep cooling process is applied to suppress the growth of these precipitates by flushing the high-temperature Er/O-doped silicon substrates with helium gas cooled in liquid nitrogen. The resultant light-emitting efficiency at room temperature is enhanced by two orders of magnitude in comparison with that of the sample treated via standard rapid thermal annealing. The deep-cooling-processed Si samples are further processed into light-emitting diodes. Bright electroluminescence with a main spectral peak at 1536 nm is also observed from the silicon-based diodes with the external quantum efficiency reaching ≈0.8% at room temperature. Based on these results, the development of electrically driven silicon optical amplifiers or even lasers at communication wavelengths is promising for monolithically integrated silicon photonics.

The monolithic integration of fiber optics with complementary metal–oxide–semiconductor (CMOS) integrated circuits will significantly speed up the computing and data transmission of current communication networks.[1–3] This technology requires efficient silicon-based light sources and optical amplifiers at communication wavelengths.[4,5] Unfortunately, silicon is an indirect bandgap semiconductor that cannot emit light at communication wavelengths. Erbium ions (Er^{3+}) have radiative emissions near 1.54 μm, which is in the telecommunication wavelength band for long-haul optic fibers.[5–8] Thus, doping silicon with Er^{3+} luminescence centers is considered a promising approach[8–10] among others[11–16] to produce silicon-based light sources. Due to their relatively low solubility ($\approx 5 \times 10^{17}$ cm^{-3}) in silicon, Er (with O) impurities are often incorporated into silicon via nonequilibrium ion implantation.[5–10] Notably, ion implantation will cause severe lattice damage, which is detrimental to high-performance electronic devices. Rapid thermal annealing (RTA) is widely employed to repair damaged lattices. However, during the standard RTA treatment, large $Er_2O_3/ErSi_{1.7}$ or similar composites precipitate out of silicon as the Er/O co-doped silicon substrate slowly cools, generating a high concentration of defects due to the lattice mismatch between the silicon lattice and the precipitates; these defects act as efficient nonradiative recombination centers.[5–10,17,18] Consequently, the emission from Er/O co-doped crystalline silicon is extremely weak at room temperature.[5–10,17,18] In the 1990s, solid phase epitaxy was employed to treat Er/O co-doped Si samples via thermal annealing at 550 °C for several hours.[19–21] In this process, the silicon amorphized via ion implantation could be recrystallized as defects migrated from the bulk to surfaces. Erbium impurities tended to move along the defects, generating a high concentration of uniformly distributed erbium impurities in silicon. Nevertheless, the thermal quenching effect remained strong, and consequently, the photoluminescence (PL) efficiency at room temperature was still low, although room-temperature PL was observed.[19–21] Here, we employ a deep cooling (DC) process for the first time to treat an Er/O-implanted Si wafer following high-temperature thermal annealing at a cooling rate of up to 1000 °C s^{-1} by flushing with helium gas cooled in liquid nitrogen (77 K). The dramatic cooling process suppresses the growth of $Er_2O_3/ErSi_{1.7}$ precipitation, enabling a strong room-temperature PL emission at 1.54 μm from the Er/O co-doped silicon wafer. The relative quantum efficiency of the emission

Dr. H. Wen, Dr. J. He, Z. Xu, Prof. H. Zhu, Prof. J. Liu, Prof. Y. Dan
National Key Laboratory of Science and Technology on Micro/Nano Fabrication Laboratory
Department of Micro/Nano Electronics
University of Michigan-Shanghai Jiao Tong University Joint Institute
Shanghai Jiao Tong University
Shanghai 200240, China
E-mail: yaping.dan@sjtu.edu.cn
J. Hong, Prof. F. Yue
Key Laboratory of Polar Materials and Devices
Ministry of Education
East China Normal University
Shanghai 200241, China
E-mail: fyyue@ee.ecnu.edu.cn
S. Jin, Prof. G. Sha
Herbert Gleiter Institute of Nanoscience
Nanjing University of Science and Technology
Nanjing 210094, China
The ORCID identification number(s) for the author(s) of this article can be found under https://doi.org/10.1002/adom.202000720.

DOI: 10.1002/adom.202000720

is approximately two orders of magnitude higher than that of the samples treated via RTA. The DC-processed Si samples are further processed into light-emitting diodes (LEDs). Bright electroluminescence (EL) with a main spectral peak at 1536 nm is also observed from the silicon-based diodes with the external quantum efficiency (EQE) reaching a record high of ≈0.8% at room temperature. Given the single-crystalline nature of the silicon substrate, efficient electrically driven optical amplifiers and even silicon lasers,[8,10,22] if equipped with a high-quality resonant cavity, may be further developed for the full integration of fiber optics with CMOS circuitry in the future.

An intrinsic single-crystalline silicon wafer was first doped with erbium and oxygen via ion implantation at a dose ratio of Er: O = 1: 2.5, which was observed to be the optimal ratio after repeating the following experiments. Secondary mass spectrometry (SIMS) measurements (Figure S1a, Supporting Information) show that Er and O dopants are mostly located 80 nm below the surface with the maximum concentrations of 7.5×10^{20} and 2.0×10^{21} cm^{-3}, respectively. The Er/O-implanted silicon wafer was subsequently cut into two sets of samples, which were then subjected to the DC and RTA treatments separately. Unlike RTA, a dramatic cooling rate of up to 1000 °C s^{-1}, following high-temperature thermal annealing, was applied to the Er/O co-doped silicon wafer by flushing with helium gas cooled in liquid nitrogen (77 K). Consequently, the DC process can largely suppress the growth of $Er_2O_3/ErSi_{1.7}$ precipitation during RTA. The detailed experimental conditions are presented in the Experimental section. Temperature-dependent PL spectra were obtained after the treatments. The inset of **Figure 1**a shows the temperature-dependent PL spectra of the DC-processed sample. The PL spectra of the RTA-processed samples are presented in Figure S2a (Supporting Information). To investigate the effect of the DC treatment, we plotted the normalized peak amplitudes at different temperatures in an Arrhenius plot (Figure 1a). The RTA-treated sample exhibited a temperature-dependent PL similar to that widely reported in the literature.[6,10,18] The PL intensity declined slightly by a factor of ≈3 as the temperature increased from 4 to ≈100 K. Subsequently, it was exponentially quenched by two orders of magnitude when the temperature further increased to room temperature. The strong thermal quenching was caused by the high density of defects in the RTA-treated sample.[9,21] In contrast, the PL intensity of the DC-processed sample maintained a weak dependence on temperature from 4 K to near room temperature. The strong thermal quenching effect from 100 to 300 K in the RTA-treated sample did not appear in the DC

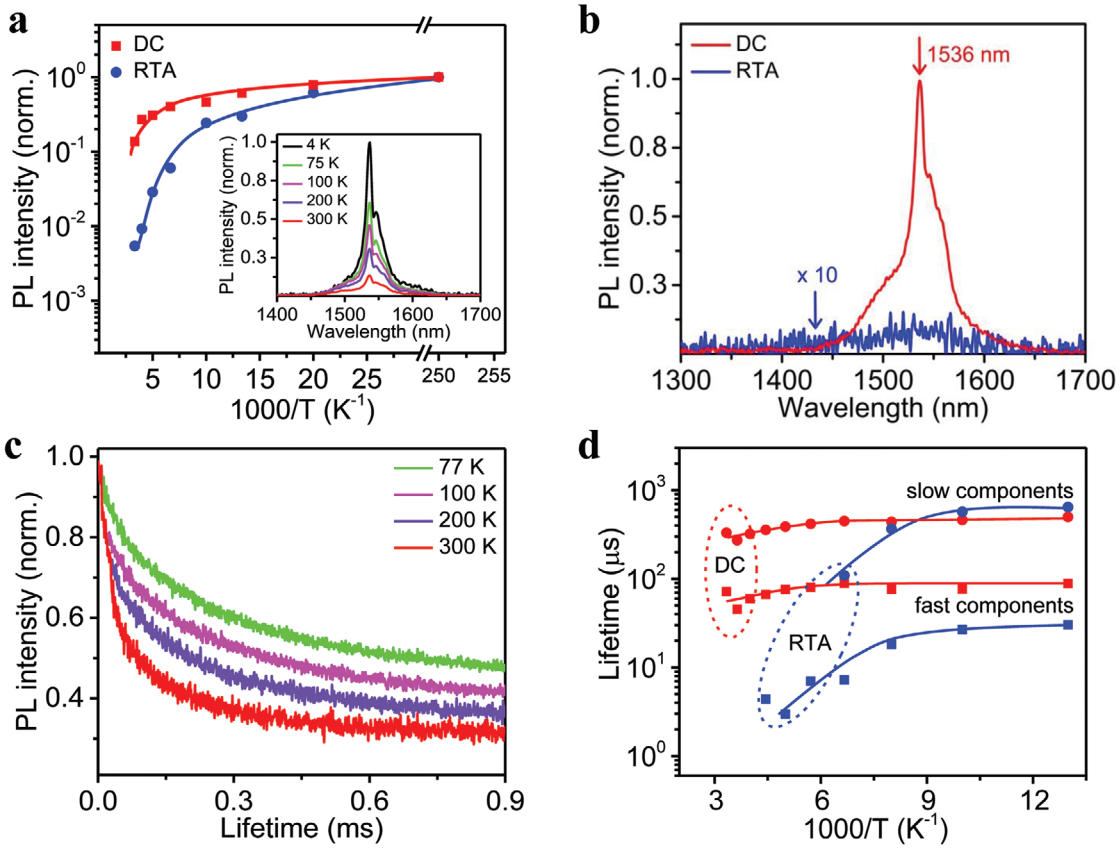

Figure 1. Temperature-dependent PL spectra of the Er/O-Si samples. a) Temperature-dependent peak amplitude at 1536 nm for DC- (red) and RTA-processed (blue) samples. Inset: the temperature-dependence of PL spectra for DC-processed samples. b) Room-temperature PL spectra for DC- (red line) and RTA-processed (blue line) samples. For comparison, the PL intensity of the RTA-processed samples was multiplied by a factor of 10. c) Temperature-dependent transient decay traces at 1536 nm for DC-processed samples (77–300 K). The excitation laser power was 400 mW at a wavelength of 405 nm. d) Fast and slow decay times as a function of temperature for DC- (red dots and squares) and RTA-processed (blue dots and squares) samples. The solid lines are used to guide the eye.

sample, indicating that the DC treatment significantly reduced the density of nonradiative defects in the Er/O-doped silicon sample.[21] Consequently, the light emission efficiency of the DC sample at room temperature was enhanced by nearly two orders of magnitude in comparison with that of the RTA sample. For a better comparison, we plotted the room-temperature PL spectra for these two samples in Figure 1b. Sharp luminescence at 1536 nm with a narrow full width at half maximum (≈25 nm)[5–10] was observed in the DC sample at room temperature. This spectral peak represents the characteristic 4f transition of Er^{3+} in Er-O-Si complexes.[7,23] In addition to the main peak at 1536 nm, we observed relatively weak shoulders at 1546 and 1554 nm due to the Stark splitting effect.[23,24]

Figure 1c shows the transient PL decay traces of the DC-processed sample after the pulsed excitation laser was turned off. The decay traces of the RTA-treated sample are shown in Figure S2b (Supporting Information). The decay traces are double exponentials consisting of fast and slow decaying components. The decay times for the fast (≈80 µs) and slow components (≈600 µs) are comparable for both samples at low temperatures (< 100 K). When the temperature was higher than 100 K, the decay times of the RTA-treated sample declined rapidly, whereas those of the DC-processed sample remained nearly constant until near room temperature. When the excitation laser was turned off, the excited Er ions could relax to ground states through either radiative emission or back transfer. A higher temperature will increase the back-transfer efficiency if there is a high density of defect states in the surrounding medium, whereas the radiative emission of excited Er ions is hardly affected by the temperature or the presence of defects in the surrounding medium.[25] The weak temperature dependence of the decay times in the DC-processed sample indicates that the DC process significantly reduced the density of nonradiative defects, consistent with the conclusion drawn from the temperature-dependent PL spectra in Figure 1a.

The strong PL indicates that the Er/O-implanted crystalline silicon can be processed into an electrically driven LED by forming a PN junction. As the Er/O impurities are donor-type dopants in silicon, a PN junction diode can be formed simply by doping the sample with boron via ion implantation. The peak concentration of boron dopants is ≈10^{19} cm^{-3} and the peak center is located ≈240 nm below the surface, ≈160 nm below the Er/O distribution peak (see Figure S1b in the Supporting Information for the boron doping profile, Supporting Information). The DC process was applied to activate the Er/O and B dopants simultaneously. A vertical PN junction diode was formed when a metal electrode was in contact with the underlying p-type silicon layer after the Er/O-doped silicon layer was removed. The 3D schematics and cross-section of the device are depicted in **Figure 2**a,b. An optical microscopic top-view of the device is shown in the inset of Figure 2c. The diode exhibits a rectifying current density versus voltage (*J*–*V*) curve (Figure 2c). When the diode is forward-biased, it has a strong emission at room temperature with the spectral characteristics of Er^{3+} ions (Figure 2d). As the injecting current increases, the emission peak at 1536 nm increases rapidly. A near-infrared (NIR) optical microscope (0.90–1.70 µm) was employed to record the device lightening-up process, as shown in Figures S3 and S4 and Videos in the Supporting Information. After further optimization, the maximum EQE of our Er/O-doped crystalline

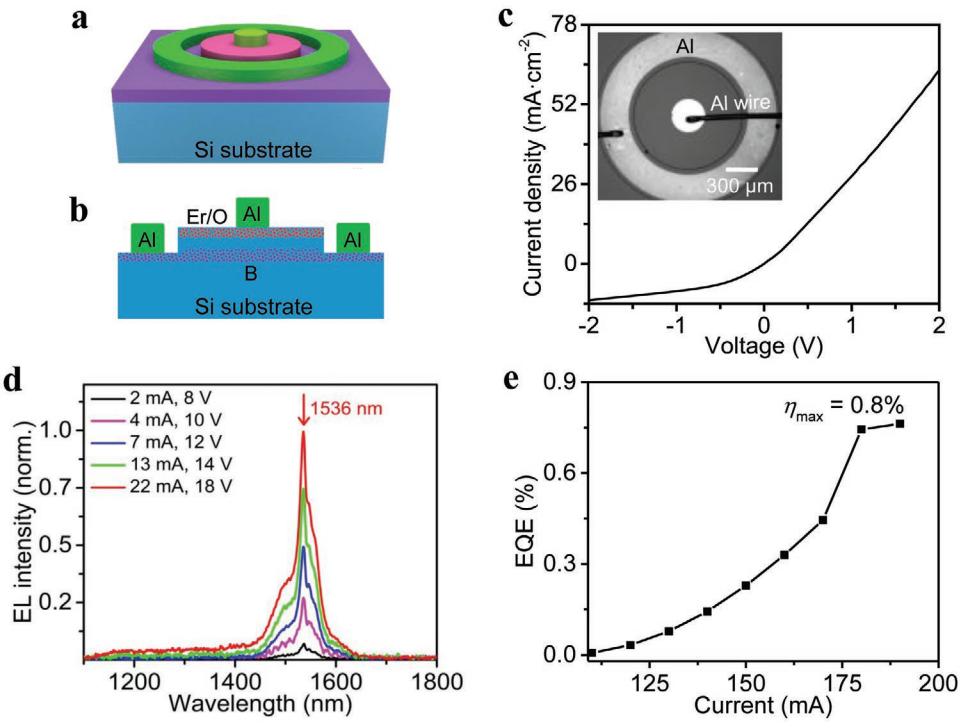

Figure 2. Optoelectronic properties of Er/O-Si LED devices treated via DC. a) 3D schematic and b) cross-sectional illustration of the device. c) *J*–*V* curve and optical microscope image (inset) of the device. d) Room-temperature EL spectra. e) Measured EQE of Er/O-Si LED devices at different injection currents (a further optimized device with a larger emitting area).

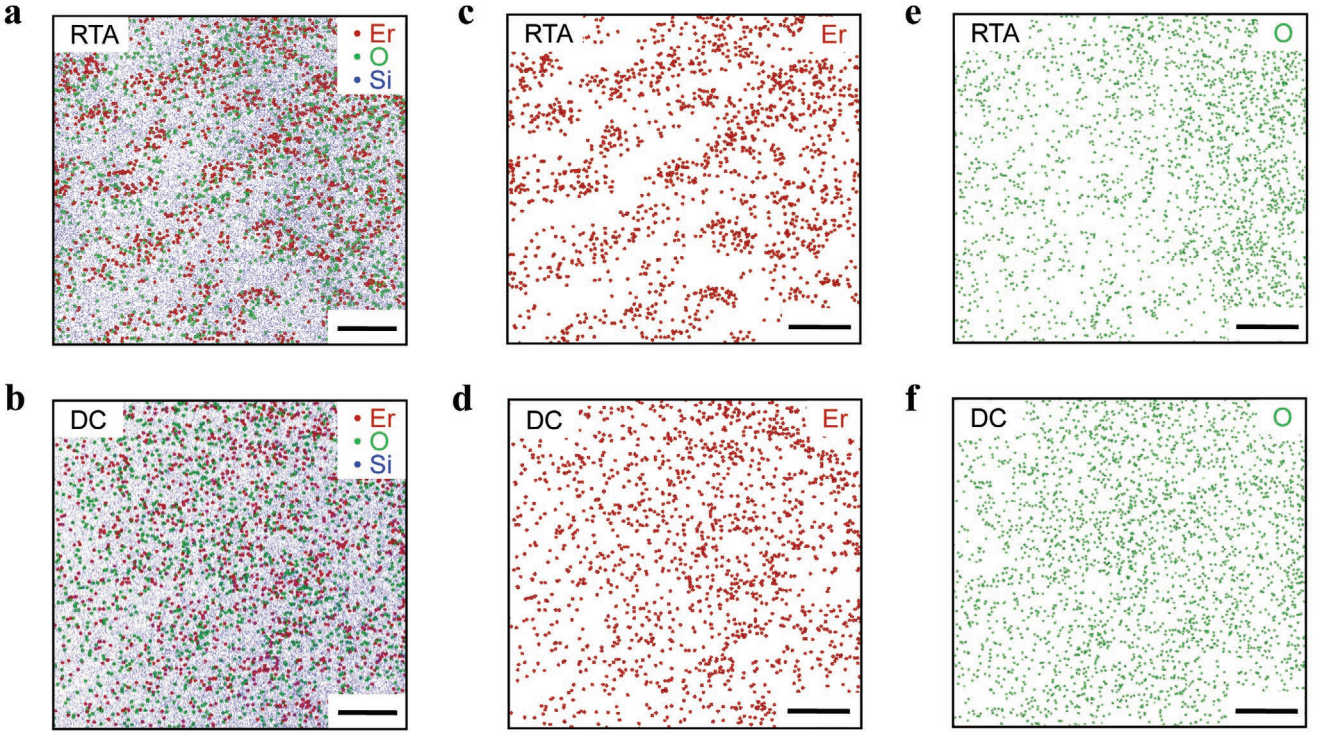

Figure 3. Er (red dots) and O (green dots) atom distributions in the Si (blue dots) matrix of the a) RTA- and b) DC-processed Er/O-Si samples obtained via APT techniques. Cartography of Er atoms (red dots) obtained from the APT analysis of the c) RTA- and d) DC-processed Er/O-Si samples. Cartography of O atoms (green dots) obtained from the APT analysis of the e) RTA- and f) DC-processed Er/O-Si samples. All scale bars are 5 nm.

silicon diodes reached ≈0.8%, which was calibrated using an integrating sphere (IS-200 Thorlabs), as shown in Figure 2e.

To understand the mechanism of the strong emission from the DC-processed sample, we used atom probe tomography (APT)[26] to map the spatial distribution of elements (Figure S5, Supporting Information) in both the DC- and RTA-processed samples for a comparison. **Figure 3**a,b shows the Si, Er, and O lateral distributions at 80 nm below the substrate surface where the Er and O dopant concentrations reached the maximum. Er atoms aggregated into large clusters in the RTA-treated sample (Figure 3c). No Er atoms were detected outside the clusters (the detection limit of APT was $\approx 10^{18}$ cm^{-3}). The aggregation of Er atoms in the DC-processed sample is not evident, and the Er clusters are much smaller (Figure 3d). The O distribution is strongly correlated with the Er distribution, particularly in the RTA-processed sample, resulting in visible O aggregation. However, the spatial distribution of O is more uniform with a relatively high concentration of O detectable outside the Er clusters (Figure 3e,f). Previously, we concluded from Figure 1a and Figure S2a (Supporting Information) that the PL peak at 1536 nm originates from Er_2O_3 or similar composites.[7,23] As the concentration of Er outside the clusters is too low, the coexistence of Er and O in the cluster must have formed Er_2O_3 or similar composites, which are the sources of light emission at 1.54 µm.

Transmission electron microscopy (TEM) was employed to examine the microstructures of the Er/O-doped silicon substrate (see the bright-field images in Figures S6 and S7 in the Supporting Information). The high-angle annular dark field (HAADF) images of the Er/O co-doped region are presented in **Figure 4**a,b for the RTA- and DC-processed samples, respectively. The TEM images show that nanosized structures are formed in the silicon lattice ≈80 nm below the silicon substrate surface. Electron energy-loss spectroscopy (EELS, Figure S8, Supporting Information) reveals the Er-$N_{4,5}$ absorption edge[27] at 168 and 176 eV, which indicates that these structures are Er-related solids, and they must be the Er clusters observed via APT analysis in Figure 3. It can be observed via visual inspection that the nanostructures are much larger in the RTA-processed sample than in the DC-treated sample. To compare the sizes of these irregular-shaped nanostructures quantitatively, we equate the irregular shapes to circles with the same area (see Figure S9 in the Supporting Information for the profile of the irregular structures, Supporting Information) and plot the histogram of the equivalent diameter in Figure 4c,d for the RTA- and DC-processed samples, respectively. The histogram shows that the nanocrystals in the RTA-processed sample are ≈3.8 ± 0.2 nm in diameter and those in the DC-processed sample are ≈1.1 ± 0.1 nm in diameter. The 3D reconstruction of the Er clusters from the APT data by properly setting the isosurfaces is presented in Figure 4e,f for the RTA- and DC-processed samples, respectively.

It is known that the solubility of Er in single-crystalline silicon is $\approx 5 \times 10^{17}$ cm^{-3} at room temperature.[9,10] Therefore, it is impossible to incorporate a high concentration of Er impurities into silicon via equilibrium approaches such as thermal diffusion or molecular beam epitaxy.[9,10,17] Ion implantation, which is a nonequilibrium approach, can introduce a high

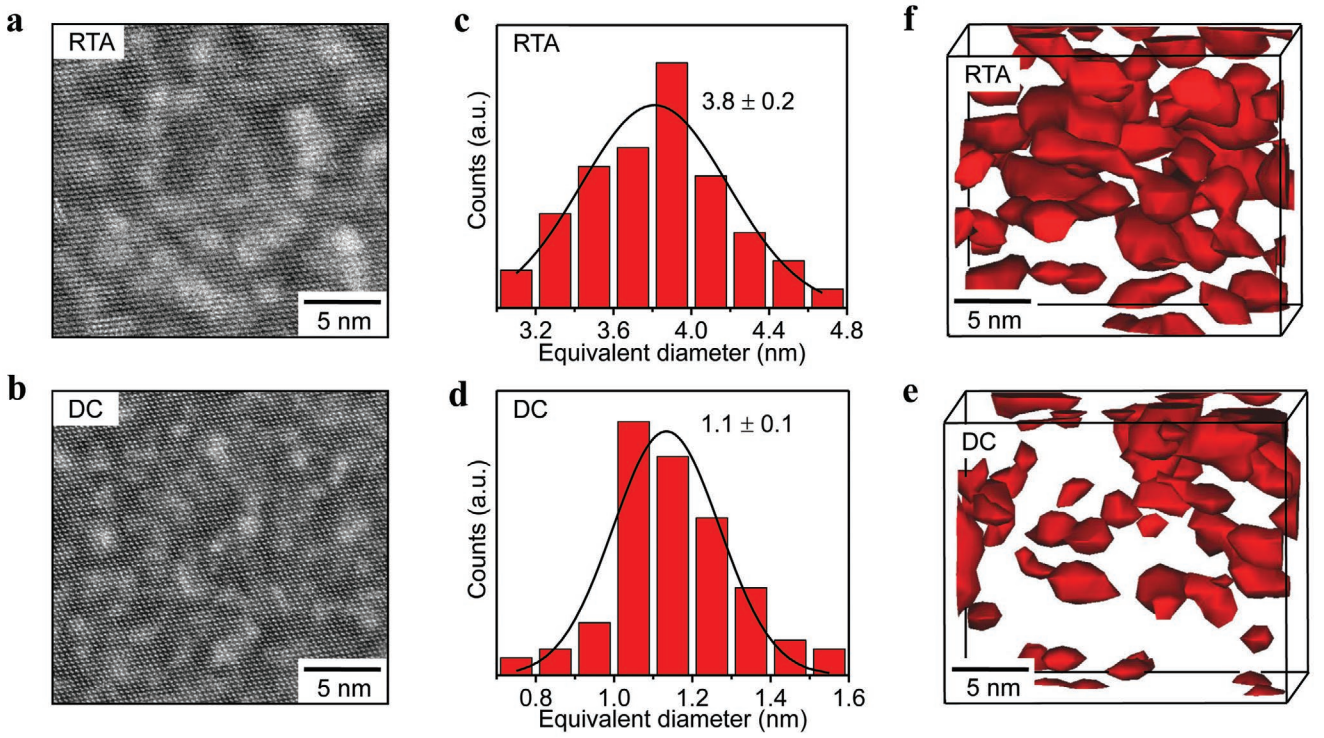

Figure 4. Microstructural characterization of the fabricated Er/O-Si samples. HAADF micrographs of the a) RTA- and b) DC-processed Er/O-Si samples. Statistical histograms of the Er nanoparticle size of the c) RTA- and d) DC-processed Er/O-Si samples. The equivalent diameters of the Er particles in (c) and (d) are ≈3.8 and 1.1 nm, respectively (the estimated errors are 0.2 and 0.1 nm in (c) and (d), respectively). 3D reconstruction with Er clusters revealed by isosurfaces at 1.5 at% Er in the e) RTA- and f) DC-processed Er/O-Si samples.

concentration of Er into silicon, but it causes lattice damage to silicon. When the temperature is increased beyond 900 °C during the thermal annealing process, the silicon atoms become mobile. Consequently, the lattice damaged by ion implantation can be fixed and the solubility of Er in silicon increases. In our case, the maximum concentrations of Er and O are of the order of 10^{20} cm^{-3}, and hence, Er and O are likely soluble in silicon at an annealing temperature of ≈950 °C, forming Er—O, Er—Si, and Si—O bonds. When the samples are cooled to room temperature, Er precipitates due to its limited solubility in silicon. Our aforementioned PL and APT analyses show that the Er precipitates contain Er_2O_3 or similar compounds. Eaglesham et al.[28] showed that Er precipitated in the form of erbium silicide ($ErSi_{1.7}$) from crystalline silicon doped solely with Er after thermal treatment. PL measurements cannot indicate the existence of erbium silicide in the precipitates, as $ErSi_{1.7}$ is not optically active even at low temperatures.[28,29] A proxigram analysis was performed on the reconstructed 3D Er clusters in Figure 4e,f to determine the chemical composition of the precipitates. The core regions of the clusters were defined by a distance of 0.4 nm to the center. The composition of the core regions was evaluated using the proxigrams (see Figure S10 in the Supporting Information). The results show that silicon atoms also exist in the clusters, but the exact ratio of silicon atoms may be difficult to determine accurately owing to the possible trajectory overlaps of the evaporated ions from the Er clusters and those from the neighboring Si matrix during field evaporation.[30] The relative ratio of Er to O atoms is reliable (**Table 1**; Table S1, Supporting Information), and it changes from 2.67 in the RTA-treated sample to 1.73 in the DC-processed sample. As the PL data show that Er binds with O in the form of Er_2O_3 or similar composites, the excess Er in the cluster must bind with silicon as erbium silicide (likely $ErSi_{1.7}$). As shown in Table 1, the ratio of Er in the erbium silicide to that in the Er_2O_3 phase, expressed as Er(Si)/Er(O), can be inferred as 3.00 and 1.59 for the RTA- and DC-processed samples, respectively.

To verify this observation, we performed in situ X-ray photoelectric spectroscopy (XPS, **Figure 5**; Figures S11–S13, Supporting Information) while removing the Er/O co-doped silicon samples layer by layer using Ar ion bombardment. At a similar depth below the surface where APT and TEM were performed, the XPS results in Figure 5 show that Er exists in the trivalent "Er(O)" and zero-valent "Er(Si)" states,[31] consistent with the above observation that Er clusters contain Er_2O_3 and erbium silicide ($ErSi_{1.7}$). The ratio of Er in the erbium silicide to that

Table 1. Elementary composition of Er nanoclusters derived from APT and XPS.

Annealing process	APT		XPS		
	Er/O	Er(Si)/Er(O)	$A_{Er(Si)}$[a)]	$A_{Er(O)}$[a)]	Er(Si)/Er(O)
RTA	2.67	3.00	16 973.68	5639.08	3.01
DC	1.73	1.59	13 595.64	7859.88	1.73

[a)]*A* denotes the integral area of Er(Si) and Er(O) at 167.70 and 170.14 eV, respectively, derived from the XPS results in Figure 5.

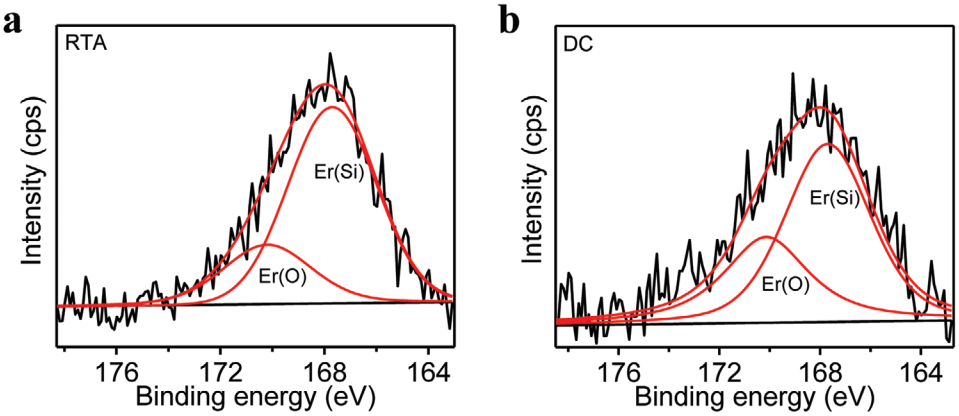

Figure 5. Dopant composition analysis of the Er/O-Si samples. Er 4d spectra of the a) RTA- and b) DC-processed Er/O-Si samples obtained ≈80 nm below the Si surface via Ar ion bombardment. The binding energies of Er(Si) and Er(O) were 167.70 and 170.14 eV, respectively.

in the Er_2O_3 phase, expressed as Er(Si)/Er(O), is 3.01 and 1.73 for the RTA- and DC-processed samples, respectively. This observation is close to the results obtained from the proxigrams (Table 1). The decrease in this ratio in the DC-processed sample is likely because erbium silicide precipitates faster than Er_2O_3, as the DC process can suppress the precipitation of erbium silicide more effectively.

The above analysis indicates that the Er/O co-doped silicon undergoes a phase transformation upon being cooled from a high temperature. Similar phenomena have been widely observed and systematically investigated in carbon steel.[32] As the sample was cooled, erbium silicide and Er_2O_3 precipitated from the silicon lattice. The standard RTA process rapidly heats but slowly cools the sample. The slow cooling process allows the precipitates to grow into large nanostructures (an equilibrium process). These nanostructures, likely crystalline, have some lattice mismatch with the surrounding silicon lattice, which can readily create a noncoherent interface.[33] The noncoherent interface induces a high concentration of interface states as efficient nonradiative recombination centers (see Note and Figures S14 and S15 in the Supporting Information). This explains the strong thermal quenching effect observed in erbium-doped silicon over the past several decades. During the DC process, the sample was cooled from 950 to –120 °C in 5 s. Although the average cooling rate is 200 °C s^{-1}, the instantaneous cooling rate at high temperature would be much faster. The ultrafast cooling does not provide sufficient time to allow the precipitation to grow (a nonequilibrium process), consistent with our APT and TEM observations. Smaller precipitates form a coherent interface with the surrounding crystalline silicon more easily, and therefore, a lower concentration of interface states is generated. Thus, the strong thermal quenching in PL can be relieved, resulting in strong light emission at room temperature from the DC-processed Si sample.

Note that the side effect of the DC process is that the thermal shock may create some dislocations and cracks in the wafer.[34] The X-ray diffraction (XRD) pattern (Figure S16, Supporting Information) shows that the silicon wafer retains a nearly perfect crystalline structure after DC treatment. Although no cracks were observed via visual inspection, bright-field TEM images show that some dislocations were formed in the silicon substrate 150 nm below the surface (denoted by the yellow dotted circle in Figure S6d in the Supporting Information). The impact of these dislocations on CMOS transistors and Si LEDs will be further evaluated. If needed, proper processes, such as a long duration of thermal treatment at relatively low temperatures, may be adopted to remove these dislocations.

In summary, Er-doped (with O) single-crystalline silicon suffers from the low solubility of Er in silicon. Although ion implantation as a nonequilibrium process can incorporate a high concentration of Er into silicon, Er will precipitate out of silicon in the equilibrium slow cooling process often performed by researchers in the past several decades.[5–10] In this work, we employed a nonequilibrium DC process to treat the Er/O co-doped single-crystalline silicon wafers. After the treatment, the precipitation of Er ions was suppressed; consequently, strong room-temperature PL at telecommunication wavelength was observed in the silicon samples. We further doped the samples with boron dopants and eventually realized an efficient room-temperature silicon LED device at 1.54 μm with an EQE reaching ≈0.8%. As these results were realized on single-crystalline silicon, the development of electrically driven optical amplifiers and even silicon lasers (if the efficiency can be further improved via process optimization) is promising for fully integrated silicon photonics in the future.[35]

Experimental Section

Preparation and Characterization: FZ intrinsic Si (100) wafers (resistivity: ≥10 kΩ cm; thickness: 500 ± 20 μm) were purchased from Suzhou Resemi Semiconductor Co., Ltd, China. The silicon wafers were first cleaned with ethanol and deionized water, and then immersed in a piranha solution (sulfuric acid: 30% hydrogen peroxide = 3:1) for 30 min at 90 °C, followed by 2.5% HF etching. Erbium and oxygen ions were implanted at the Institute of Semiconductors, Chinese Academy of Sciences in Beijing, China. The injection energies and doses of Er and O ions were 200 keV, 4×10^{15} cm^{-2}, and 32 keV, 10^{16} cm^{-2}, respectively. After the implantation, the Er/O-implanted silicon samples were subjected to the aforementioned cleaning procedure again before the deposition of a 200-nm-thick SiO_2 film via reactive magnetron sputtering (Delton multi-target magnetic control sputtering system, AEMD, SJTU). The DC and standard RTA processes were applied to the two Er/O co-doped silicon samples separately. PL characterizations were performed after

the capping of the SiO_2 film was removed in a buffered oxide etchant solution.

As shown in Figure S1a (Supporting Information), the SIMS technique (Evans Analytical Group, NJ, USA) was subsequently utilized to characterize the Er and O dopant distribution profiles at the top 300 nm of the silicon substrate. For the Er element, the SIMS data are the summation of three Er isotopes (166, 167, and 168). For the O element, no other isotopes were detected. The bump near the surface (green line) likely originates from the contamination of native silicon oxide. To form a PN junction, boron dopants were later implanted into the Si substrate (see the section of LED fabrication and imaging). The SIMS profile of boron dopants is shown in Figure S1b (Supporting Information).

Deep Cooling and RTA Processes: The DC process was performed on the Er/O-Si samples in an upgraded dilatometer (DIL 805A, TA Instruments), in which the samples were annealed at 950 °C for 5 min at a pressure of 5×10^{-4} mbar via copper-coil-based electromagnetic heating, followed by flushing with high-purity He (99.999%) gas cooled in liquid N_2 (77 K). A K-type thermocouple was utilized to control the real-time temperature accurately by tuning the flow rate of He gas from 100–300 mL s^{-1} during the DC process. The silicon samples were cooled to room temperature in less than 5 s. The RTA procedure for the Er/O-Si samples was first conducted in a rapid thermal processing furnace (RTP-300) at 1050 °C for 5 min. After the high-temperature treatment, the silicon samples were gradually cooled with high-purity N_2 gas.

PL Measurements: The PL measurements were performed using a Fourier-transform infrared (FTIR) spectrometer (Vertex 80 V, Bruker) equipped with a liquid-nitrogen-cooled Ge detector. A CW diode laser with λ = 405 nm (MLL-III-405, CNI, Changchun, China) providing a maximum excitation power of ≈150 mW was employed as the excitation source. During the measurements, the Er/O-Si samples were mounted on the cold head of a helium closed-cycle cryostat (DE-202S, ARS), which allowed for a temperature adjustment from 4 K to ambient temperature (Figure 1a; Figure S2a, Supporting Information). Time-resolved PL measurements were performed using an Edinburg FLS1000 fluorescence spectrometer, where a nanosecond pulse laser (MDL-NS-405, CNI, Changchun, China) acted as the source of excitation.

LED Fabrication, Emission, and Imaging: To form a PN junction on the Er/O co-doped silicon wafers, boron ions were implanted (80 keV and 5.2×10^{14} cm^{-2}) into the silicon wafer with a peak concentration located ≈240 nm below the surface (Figure S1b, Supporting Information). All the dopants were simultaneously activated in the subsequent DC process. As the Er/O dopants (donors) were located in a shallower layer, a vertical PN junction was formed between the n-type Er/O layer and the p-type B doping layer. A pair of co-axial electrodes was formed via UV photolithography (MDA-400M, MIDAS), deep silicon etching (SPTS ICP), and metal film deposition (Nexdep, Angstrom Engineering Inc.). As shown in Figure 2a,b the internal electrode is in contact with the n-type Er/O doping region and the external electrode is in contact with the p-type region after the top Er/O layer is removed via deep silicon etching. All the microfabrication processes were performed at the Center for Advanced Electronic Materials and Devices, Shanghai Jiao Tong University.

After Al metal wire bonding (7476D, West Bond), the devices were integrated on a PCB board. The *J–V* curves (Figure 2c) of the Er/O-Si LED devices were measured using a digital sourcemeter (Keithley 2400) controlled by a Labview script. For EL measurements (Figure 2d), the devices were electrically pumped by the sourcemeter and the emission spectra were collected using the same FTIR system for PL measurements. In addition, an integrating sphere equipped with the Edinburg FLS1000 instrument was used to estimate the EL efficiency at room temperature, after the optical property of the integrating sphere was carefully characterized. NIR imaging of the emission from the Er/O-Si LED device was performed at room temperature under an optical microscope (BX53M, Olympus) equipped with an NIR camera (C12471-03, Hamamatsu). The setup is shown in Figure S3 (Supporting Information). The recorded photographs and videos are shown in Figure S4 and Video in the Supporting Information.

Microstructure and Composition Characterizations: The microstructure and composition of the Er/O-Si samples were fully investigated using APT, TEM, XPS, and XRD. The APT specimens were prepared using a focused ion beam (FIB, Zeiss Auriga SEM/FIB) following a standard lift-out procedure.[36] The APT analysis for the 3D distribution of elements in the materials was performed using a CAMECA local electrode atom probe LEAPTM 4000X SI at a target specimen temperature of 20 K, under a pulsing UV laser with a pulse energy of 40 pJ, a pulse rate of 200 kHz, and an ion collection rate of 0.5% per pulse. The APT data were reconstructed and quantitatively analyzed using CAMECA IVAS version 3.6.8 software. The compositions of the Er nanoclusters were estimated by averaging the core concentrations of the proximity histograms produced by reconstructing 1.5% (in at%) isoconcentration surfaces in the DC- and RTA-processed samples.

Talos F200X field-emission TEM was employed to obtain the TEM images (Figures S6–S9, Supporting Information) of a sample slide cut from the samples using a focused ion beam (FIB, GAIA3 GMU Model 2016). For energy-dispersive X-ray (EDX) mapping measurements, the acceleration voltage was 200 kV, and the other parameters were set as default. High-resolution TEM images were further obtained with a JEOL JEM-ARM200F, as shown in Figure 4 and Figures S7–S9 (Supporting Information). XPS was performed on a Krato AXIS UltraDLD spectrometer with a monochromated Al Ka source, a hybrid magnification mode analyzer, and a multichannel detector at a take-off angle of 90° from the silicon surface plane. In situ XPS measurements were obtained by removing the Er/O-Si surface layer using the Ar ion bombardment technique. XRD patterns were acquired using a polyfunctional X-ray diffractometer (D8 advance, Bruker), as shown in Figure S16 (Supporting Information). For a comparison, the XRD patterns of the intrinsic and Er/O-implanted Si samples without any thermal treatment were also collected.

Supporting Information

Supporting Information is available from the Wiley Online Library or from the author.

Acknowledgements

H.W., J.J.H., and J.H. contributed equally to this work. This work was supported by the special-key project of the "Innovative Research Plan," Shanghai Municipality Bureau of Education (2019-01-07-00-02-E00075), the National Science Foundation of China (21703140, 61376001, 61874072, and 61874043), and the China Postdoctoral Science Foundation (2016M601582). The authors thank Jianming Li (Institute of Semiconductors, CAS) for the ion implantation processing and Yihua Chen (Shanghai Jiao Tong Univ.) for the deep cooling treatment. The authors also thank Xuecheng Fu (Shanghai Jiao Tong Univ.) for the SiO_2 film deposition, Weiwei Wang (Spark Electro-Optics Co., Ltd.), and Lin Zhu (Cinv Co., Ltd) for their support in quantum efficiency and NIR imaging measurements.

Conflict of Interest

The authors declare no conflict of interest.

Keywords

deep cooling, erbium dopants, light-emitting diodes, near-infrared radiation, silicon photonics

Received: April 29, 2020
Revised: June 23, 2020
Published online: July 8, 2020

[1] A. H. Atabaki, S. Moazeni, F. Pavanello, H. Gevorgyan, J. Notaros, L. Alloatti, M. T. Wade, C. Sun, S. A. Kruger, H. Meng, K. A. Qubaisi, I. Wang, B. Zhang, A. Khilo, C. V. Baiocco, M. A. Popvić, V. M. Stojanović, R. J. Ram, *Nature* **2018**, *556*, 349.
[2] H. Subbaraman, X. Xu, A. Hosseini, X. Zhang, Y. Zhang, D. Kwong, R. T. Chen, *Opt. Express* **2015**, *23*, 2487.
[3] D. A. B. Miller, *Proc. IEEE* **2009**, *97*, 1166.
[4] D. Liang, J. E. Bowers, *Nat. Photonics* **2010**, *4*, 511.
[5] H. Ennen, J. Schneider, G. Pomrenke, A. Axmann, *Appl. Phys. Lett.* **1983**, *43*, 943.
[6] F. Priolo, G. Franzò, S. Coffa, A. Carnera, *Phys. Rev. B* **1998**, *57*, 4443.
[7] M. A. Lourenço, M. M. Milošević, A. Gorin, R. M. Gwilliam, K. P. Homewood, *Sci. Rep.* **2016**, *6*, 37501.
[8] Z. Zhou, B. Yin, J. Michel, *Light: Sci. Appl.* **2015**, *4*, e358.
[9] A. J. Kenyon, *Semicond. Sci. Technol.* **2005**, *20*, R65.
[10] A. Polman, *J. Appl. Phys.* **1997**, *82*, 1.
[11] Y. Takahashi, Y. Inui, M. Chihara, T. Asano, R. Terawaki, S. Noda, *Nature* **2013**, *498*, 470.
[12] H. Rong, A. Liu, R. Jones, O. Cohen, D. Hak, R. Nicolaescu, A. Fang, M. Paniccia, *Nature* **2005**, *433*, 292.
[13] Y. Sun, K. Zhou, Q. Sun, J. Liu, M. Feng, Z. Li, Y. Zhou, L. Zhang, D. Li, S. Zhang, M. Ikeda, S. Liu, H. Yang, *Nat. Photonics* **2016**, *10*, 595.
[14] S. Chen, W. Li, J. Wu, Q. Jiang, M. Tang, S. Shutts, S. N. Elliott, A. Sobiesierski, A. J. Seeds, I. Ross, P. M. Smowton, H. Liu, *Nat. Photonics* **2016**, *10*, 307.
[15] J. Liu, X. Sun, R. Camacho-Aguilera, L. C. Kimerling, J. Michel, *Opt. Lett.* **2010**, *35*, 679.
[16] D.-C. Wang, C. Zhang, P. Zeng, W.-J. Zhou, L. Ma, H.-T. Wang, Z.-Q. Zhou, F. Hu, S.-Y. Zhang, M. Lu, X. Wu, *Sci. Bull.* **2018**, *63*, 75.
[17] V. P. Kuznetsov, R. A. Rubtsova, V. N. Shabanov, A. P. Kasatkin, S. V. Sedova, G. A. Maksimov, Z. F. Krasil'nik, E. V. Demidov, *Phys. Solid State* **2005**, *47*, 102.
[18] S. Scalese, G. Franzò, S. Mirabella, M. Re, A. Terrasi, F. Priolo, E. Rimini, C. Spinella, A. Camera, *J. Appl. Phys.* **2000**, *88*, 4091.
[19] A. Polman, J. S. Custer, E. Snoeks, G. N. van den Hoven, *Appl. Phys. Lett.* **1993**, *62*, 507.
[20] J. S. Custer, A. Polman, H. M. van Pinxteren, *J. Appl. Phys.* **1994**, *75*, 2809.
[21] F. Priolo, G. Franzò, S. Coffa, A. Polman, S. Libertino, R. Barklie, D. Carey, *J. Appl. Phys.* **1995**, *78*, 3874.
[22] J. D. B. Bradley, M. Pollnau, *Laser Photonics Rev.* **2011**, *5*, 368.
[23] M. Miritello, R. Lo Savio, A. M. Piro, G. Franzò, F. Priolo, F. Iacona, C. Bongiorno, *J. Appl. Phys.* **2006**, *100*, 013502.
[24] J. Li, Q. Lin, Z. Sun, *J. Lumin.* **2012**, *132*, 325.
[25] N. Hamelin, P. G. Kik, J. F. Suyver, K. Kikoin, A. Polman, A. Schönecker, F. W. Saris, *J. Appl. Phys.* **2000**, *88*, 5381.
[26] G. Beainy, C. Frilay, P. Pareige, F. Gourbilleau, E. Talbot, *J. Alloys Compd.* **2018**, *755*, 55.
[27] R. J. Kashtiban, U. Bangert, I. Crowe, M. P. Halsall, B. Sherliker, A. J. Harvey, J. Eccles, A. P. Knights, R. Gwilliam, M. Gass, *J. Phys.: Conf. Ser.* **2010**, *209*, 012043.
[28] D. J. Eaglesham, J. Michel, E. A. Fitzgerald, D. C. Jacobson, J. M. Poate, J. L. Benton, A. Polman, Y.-H. Xie, L. C. Kimerling, *Appl. Phys. Lett.* **1991**, *58*, 2797.
[29] A. Terrasi, G. Franzò, S. Coffa, F. Priolo, F. D'Acapito, S. Mobilito, *Appl. Phys. Lett.* **1997**, *70*, 1712.
[30] G. Sha, A. Cerezo, *Ultramicroscopy* **2005**, *102*, 151.
[31] N. Guerfi, T. A. N. Tan, J. Y. Veuillen, D. B. Lollman, *Appl. Surf. Sci.* **1992**, *56–58*, 501.
[32] N. S. Kalsi, R. Sehgal, V. S. Sharma, *Mater. Manuf. Processes* **2010**, *25*, 1077.
[33] V. Popescu, A. Zunger, *Phys. Rev. B* **2011**, *84*, 125315.
[34] W. L. Ng, M. A. Lourenço, R. M. Gwilliam, S. Ledain, G. Shao, K. P. Homewood, *Nature* **2001**, *410*, 192.
[35] D. Thomson, A. Zilkie, J. E. Bowers, T. Komljenovic, G. T. Reed, L. Vivien, D. Marris-Morini, E. Cassan, L. Virot, J.-M. Fédéli, J.-M. Hartmann, J. H. Schmid, D.-X. Xu, F. Boeuf, P. O'Brien, G. Z. Mashanovich, M. Nedeljkovic, *J. Optics* **2016**, *18*, 073003.
[36] K. Thompson, D. Lawrence, D. J. Larson, J. D. Olson, T. F. Kelly, B. Gorman, *Ultramicroscopy* **2007**, *107*, 131.